Supplemental Information for:

Noncovalent immobilization and surface characterization of lanthanide complexes on carbon electrodes

*Davide Lionetti, Victor W. Day, and James D. Blakemore**

Department of Chemistry, University of Kansas
1251 Wescoe Hall Drive, Lawrence, KS 66045

*To whom correspondence should be addressed: blakemore@ku.edu

Contents

Experimental Details

Experimental Details

General considerations

All manipulations were carried out in dry N_2-filled gloveboxes (Vacuum Atmospheres Co., Hawthorne, CA) or under N_2 atmosphere using standard Schlenk techniques unless otherwise noted. All solvents were of commercial grade and dried over activated alumina using a PPT Glass Contour (Nashua, NH) solvent purification system prior to use, and were stored over molecular sieves. All chemicals were from major commercial suppliers and used as received after extensive drying. Deuterated NMR solvents were purchased from Cambridge Isotope Laboratories; CD_2Cl_2 was dried over CaH_2. 3-(chloromethyl)-2-hydroxy-5-methylbenzaldehyde (**1**) and *N*-methyl-1-(pyren-1-yl)methanamine were synthesized accordingly to previously published procedures.[1-2] Complexes $M(N(SiMe_3)_2)_3$ (M = Ce, Nd, Sm, Eu), $\mathbf{L^{tBu}Ce}$, and $\mathbf{L^{tBu}Eu}$ were prepared according to the literature.[3] ^1H and ^{13}C NMR spectra were collected on 400 or 500 MHz Bruker spectrometers and referenced to the residual protio-solvent signal[4] in the case of ^1H and ^{13}C or the deuterium lock signal in the case of ^{19}F and ^{31}P. Chemical shifts (δ) are reported in units of ppm and coupling constants (J) are reported in Hz. Elemental analyses were performed by Midwest Microlab, Inc. (Indianapolis, IN).

Electrochemistry

Electrochemical experiments were carried out in a nitrogen-filled glove box. 0.10 M tetra(n-butylammonium) hexafluorophosphate (Sigma-Aldrich; electrochemical grade) in acetonitrile served as the supporting electrolyte. Measurements were made with a Gamry Reference 600 Plus Potentiostat/Galvanostat using a standard three-electrode configuration. For solution experiments, the working electrode was the basal plane of highly oriented pyrolytic graphite (HOPG) (GraphiteStore.com, Buffalo Grove, Ill.; surface area: 0.09 cm^2), the counter electrode was a platinum wire (Kurt J. Lesker, Jefferson Hills, PA; 99.99%, 0.5 mm diameter), and a silver wire immersed in electrolyte served as a pseudo-reference electrode (CH Instruments). The reference was separated from the working solution by a Vycor frit (Bioanalytical Systems, Inc.). Ferrocene (Sigma Aldrich; twice-sublimed) was added to the electrolyte solution at the conclusion of each experiment (~1 mM); the midpoint potential of the ferrocenium/ferrocene couple (denoted as $Fc^{+/0}$) served as an external standard for comparison of the recorded potentials. Concentrations of analyte for solution cyclic voltammetry were typically 2 mM. For cyclic voltammetry measurements on surface-immobilized complexes, the working electrode consisted of a 1 cm^2 block of HOPG prepared with carbon black on the basal plane as described in the literature.[5-7] The electrode was secured in a custom-made Teflon cell with an O-ring seal used to define the geometric area of the electrode (0.28 cm^2). The counter and quasi-reference electrodes were as described for solution experiments. The ferrocenium/ferrocene couple was used as an external reference in all experiments to calibrate potentials.

X-ray photoelectron spectroscopy (XPS)

X-ray photoelectron spectra were collected with a Physical Electronics (Phi) VersaProbe II system or a Kratos AXIS Ultra system. The sample chamber in both cases was kept at $<5 \times 10^{-9}$ torr. For the Phi system, ejected electrons are collected at an angle of 45° from the surface normal. For the Kratos system, ejected electrons are collected at an angle of 90° from the surface normal. Survey scans were performed to identify the elements on the surface of carbon electrodes, while additional high-resolution spectra were obtained for details on specific elements.

The XPS data were analysed using the program Computer Aided Surface Analysis for X-ray Photoelectron Spectroscopy (CasaXPS; from Casa Software Ltd., Teignmouth, UK). All XPS signals reported here are binding energies and are reported in eV. Backgrounds were fit with standard Shirley or linear backgrounds. Element peaks were fit with a standard Gaussian-Lorentzian line shape. For M 3d and 4d high-resolution spectra, the major features were best fit as the respective M $nd_{5/2}$ and $nd_{3/2}$ signals with constrained peak areas of 3:2 as predicted from theory.[8] Any additional features (shake-up and shake-down peaks) were modelled as distinct individual contributions. For high-resolution spectra of the N 1s regions, the data were best fit as three distinct contributions with peak areas constrained to a 3:3:1 ratio. For all spectra, fits were only constrained based on peak area.

Synthetic procedures

Synthesis of 2

In a 50 mL roundbottom flask, 3-(chloromethyl)-2-hydroxy-5-methylbenzaldehyde (0598 g, 3.24 mmol) was dissolved in THF. *N*-methyl-1-(pyren-1-yl)methanamine (0.834 g, 3.4 mmol, 1.05 equiv.) dissolved in THF was added, and a colorless precipitate formed. Triethylamine (1.8 mL, 12.95 mmol, 4 equiv.) was added dropwise, resulting in a slight change in color of the suspension to brighter yellow. The reaction mixture was stirred for 12 hours and filtered to remove the $[Et_3NH][Cl]$ byproduct, and the volatiles were removed *in vacuo*. The tile compound was obtained as a yellow oil that solidified upon standing (1.133 g, 89% yield). ^{1}H NMR (500 MHz, $CDCl_3$) δ 10.17 (s, 1H, ArC*H*O), 8.40 (d, *J* = 9.2 Hz, 1H), 8.30 – 7.90 (m, 8H), 7.34 (d, *J* = 2.2 Hz, 1H, Ar*H*), 7.21 (d, *J* = 2.2 Hz, 1H, Ar*H*), 4.31 (s, 2H, NCH_2), 3.82 (s, 2H, NCH_2), 2.34 (s, 3H, NCH_3), 2.24 (s, 3H, ArCH_3) ppm. ^{13}C NMR (126 MHz, $CDCl_3$) δ 192.85 (Ar*C*HO), 158.97, 137.14, 131.40, 131.31, 130.99, 130.93, 130.04, 129.23, 128.62, 128.51, 127.98, 127.62, 127.49, 126.15, 125.45, 125.43, 125.22, 124.94, 124.90, 124.62, 123.39, 122.09, 60.23 (N*C*H_2), 58.21 (N*C*H_2), 42.16 (N*C*H_3), 20.40 (Ar*C*H_3) ppm.

Synthesis of $L^{Pyr}H_3$

In a 50 mL roundbottom flask, aldehyde **2** (1.067 g, 2.71 mmol) was dissolved in CH_2Cl_2. Sodium sulfate (10 equiv.) was added to the flask, and tris(2-aminoethyl)amine (0.132 g, 0.94 mmol, 0.33 equiv) was then added via syringe. The mixture was stirred for 12 hours, and the sodium sulfate removed via filtration through a Celite pad. The volatiles were removed *in vacuo* to give a thick yellow oil. Extensive drying at reduced pressure eventually led to foaming of the oil to give a solid material (1.08 g, 90% yield). ^{1}H NMR (500 MHz, $CDCl_3$) δ 14.00 (s, 3H, ArOH), 8.42 (d, *J* = 9.2 Hz, 3H), 8.16 – 7.89 (m, 24H), 7.76 (s, 3H, ArC*H*N), 7.23 (d, *J* = 2.4 Hz, 3H, Ar*H*), 5.84 (d, *J* = 2.3 Hz, 3H, Ar*H*), 4.20 (s, 6H, NCH_2), 3.77 (s, 6H, NCH_2), 3.50 (t, *J* = 4.8 Hz, 6H, NCH_2CH$_2$N), 2.83 (t, *J* = 5.1 Hz, 6H, NCH$_2$CH_2N), 2.25 (s, 9H, NCH_3), 2.01 (s, 9H, ArCH_3). ^{13}C NMR (126 MHz, $CDCl_3$) δ 166.35 (Ar*C*HN), 157.74, 134.36, 133.27, 131.38, 131.01, 130.73, 130.58, 129.99, 128.23, 127.54, 127.08, 127.03, 126.91, 126.03, 125.82, 125.09, 124.95, 124.93, 124.89, 124.44, 124.36, 118.20, 60.35 (N*C*H_2), 58.11 (N*C*H_2), 56.29 (N*C*H_2), 55.55 (N*C*H_2), 42.61 (N*C*H_3), 20.43 (Ar*C*H_3).

General procedure for synthesis of $L^{Pyr}M$ complexes

To metallate the pyrene-appended ligand, THF solutions of $\mathbf{L^{Pyr}H_3}$ and the desired $M(N(SiMe_3)_2)_3$ precursor (1:1 stoichiometry) were frozen in a LN_2-refrigerated cold well. Upon thawing, the metal tris(amide) solution was added to the solution of ligand dropwise. The reaction mixture was stirred at room temperature until a precipitate formed (usually 12-24 hours). The mixture was filtered on a medium-porosity glass frit, and the solid washed extensively with THF. The solid was then collected and dried *in vacuo* to remove any volatiles.

$L^{Pyr}Ce$

Isolated as a light orange solid (81%).^{1}H NMR (400 MHz, CD_2Cl_2): δ 16.76 (s), 10.16 (s), 8.49 (s), 8.15 (dd, *J* = 7.6, 1.1 Hz), 8.05 (dd, *J* = 7.8, 1.2 Hz), 8.01-7.91 (m), 7.77-7.61 (m), 6.92 (d, 7.8 Hz), 3.44 (s), 2.53 (br s), 1.88 (br s), 1.60 (br s), 0.00 (s), -6.33 (s). ppm. HRMS (ESI) calcd. for $C_{87}H_{83}CeN_7O_5$ $[M+2H_2O+H]^+$: 1445.5510; Found: 1445.4938. Anal. Calcd. for $C_{87}H_{82}N_7CeO_5$ $[L^{Pyr}Ce+2H_2O]$: C 72.28, H 5.52, N 6.78; Found: C 72.28, H 5.57, N 6.83.

$L^{Pyr}Nd$

Isolated as an off-white solid (77%). ^{1}H NMR (400 MHz, CD_2Cl_2): δ 27.62 (br), 11.32 (s), 9.20 (s), 8.08-7.54 (m), 6.43 (br d, 7.8 Hz), 3.78 (s), 1.26 (br), –1.02 (s), –1.14 (br), –8.40 (br) ppm. HRMS (ESI) calcd. for $C_{87}H_{78}NdN_7O_5$ $[M+2H_2O+H]^+$: 1449.5689; Found: 1449.4994. Anal. Calcd. for $C_{87}H_{82}N_7NdO_5$ $[L^{Pyr}Nd+2H_2O]$: C 72.07, H 5.70, N 6.76; Found: C 71.76, H 5.35, N 6.69.

$L^{Pyr}Sm$

Isolated as an off-white solid (83%).^{1}H NMR (400 MHz, CD_2Cl_2): δ 8.2-7.8 (m), 7.57 (d, 2.5 Hz), 7.48 (d, 7.8 Hz), 7.07 (d, 2.5 Hz), 3.29 (br s), 2.72 (br s), 2.44 (br s), 2.32 (s), 1.26 (s), –0.84 (br s) ppm. HRMS (ESI) calcd. for $C_{87}H_{79}SmN_7O_3$ $[M+H]^+$: 1421.5442; Found: 1421.5342. Anal. Calcd. for $C_{87}H_{78}N_7O_3Sm$: C 73.59, H 5.54, N 6.90; Found: C 72.92, H 5.68, N 6.89.

$L^{Pyr}Eu$

Isolated as an off-white solid (87%).^{1}H NMR (400 MHz, CD_2Cl_2): δ 18.71 (br s), 9.15 (br, overlapping), 8.94 (d, 9.1 Hz), 8.80 (d, 7.8 Hz), 8.29 (d, 7.7 Hz), 8.16-7.92 (m), 7.97 (br, overlapping), 6.69 (br), 6.05 (br), 5.09 (s), 4.02 (s), 1.97 (s), 1.45 (s), –0.15 (s), –24.65. ppm. HRMS (ESI) calcd. for $C_{87}H_{79}EuN_7O_3$ $[M+H]^+$: 1422.5457; Found: 1422.5360. Anal. Calcd. for $C_{87}H_{78}EuN_7O_3$: C 73.51, H 5.53, N 6.90; Found: C 72.89, H 5.61, N 6.92.

Electrochemistry

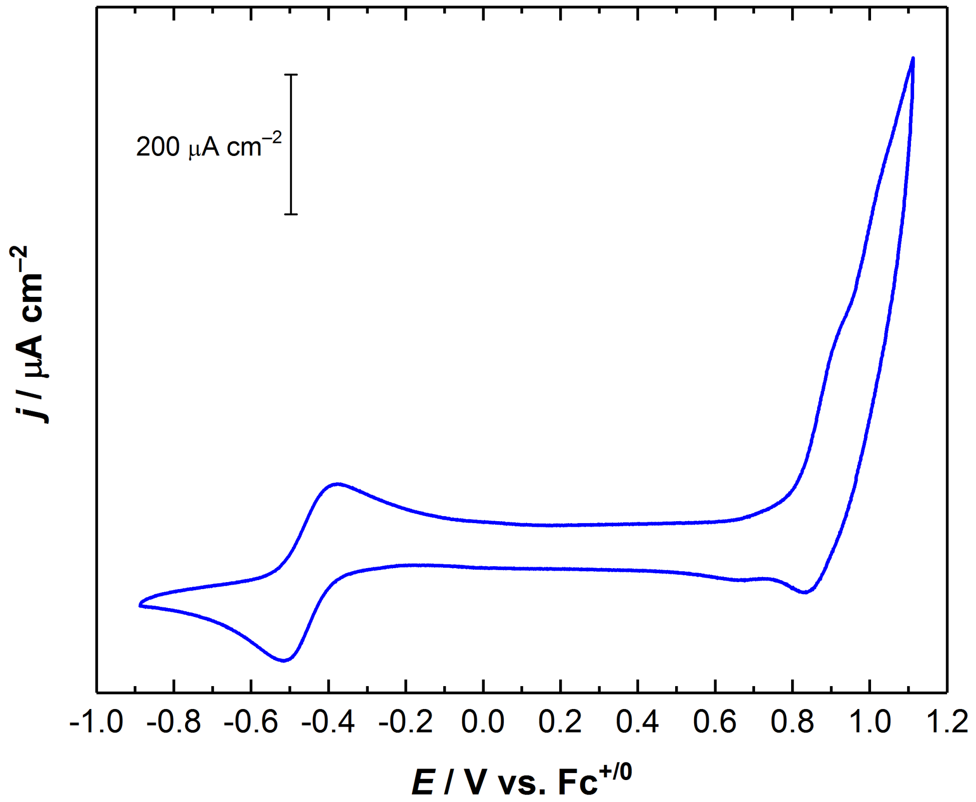

Figure S1. Extended cyclic voltammetry data for complex **L^{tBu}Ce** in CH_3CN (0.1 M [^{n}Bu$_4$N][PF_6], 100 mV/s).

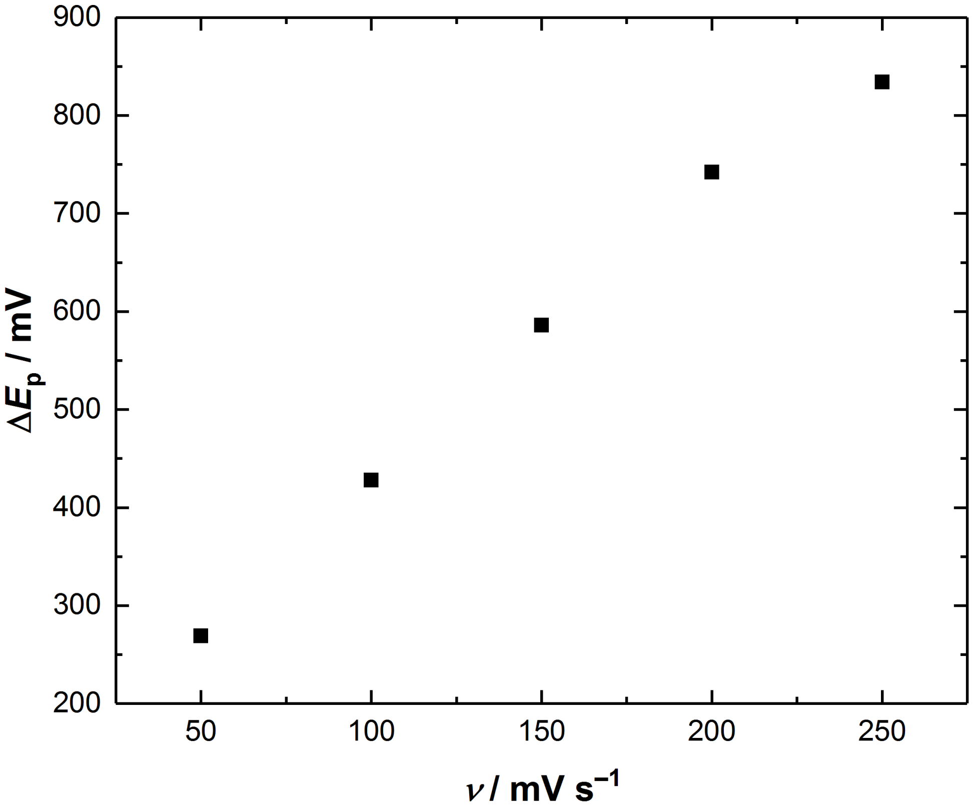

Figure S2. Plot of peak separation (ΔE_p) vs. scan rate for **L^{Pyr}Ce** immobilized on Ketjen black electrode (0.1 M [$^{n}Bu_4N$][PF_6] in CH_3CN).

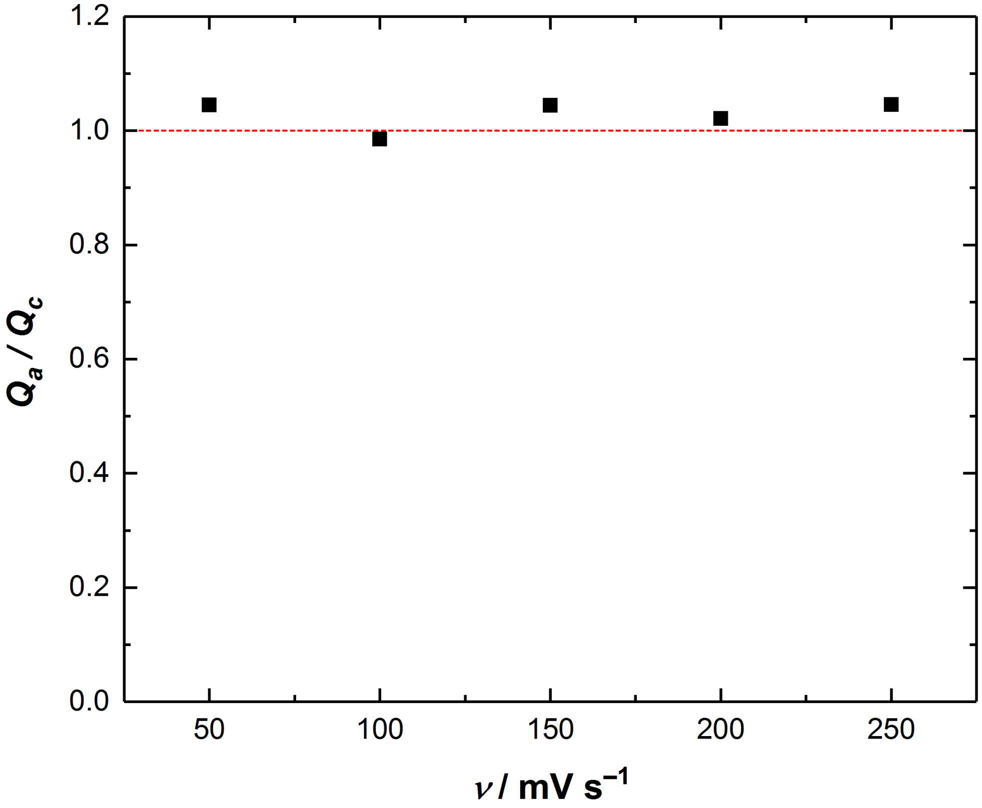

Figure S3. Plot of ratio of cathodic/anodic charge passed (Q_c/Q_a) as a function of scan rate for **L^{Pyr}Ce** immobilized on Ketjen black electrode (0.1 M [^{n}Bu$_4$N][PF$_6$] in CH$_3$CN).

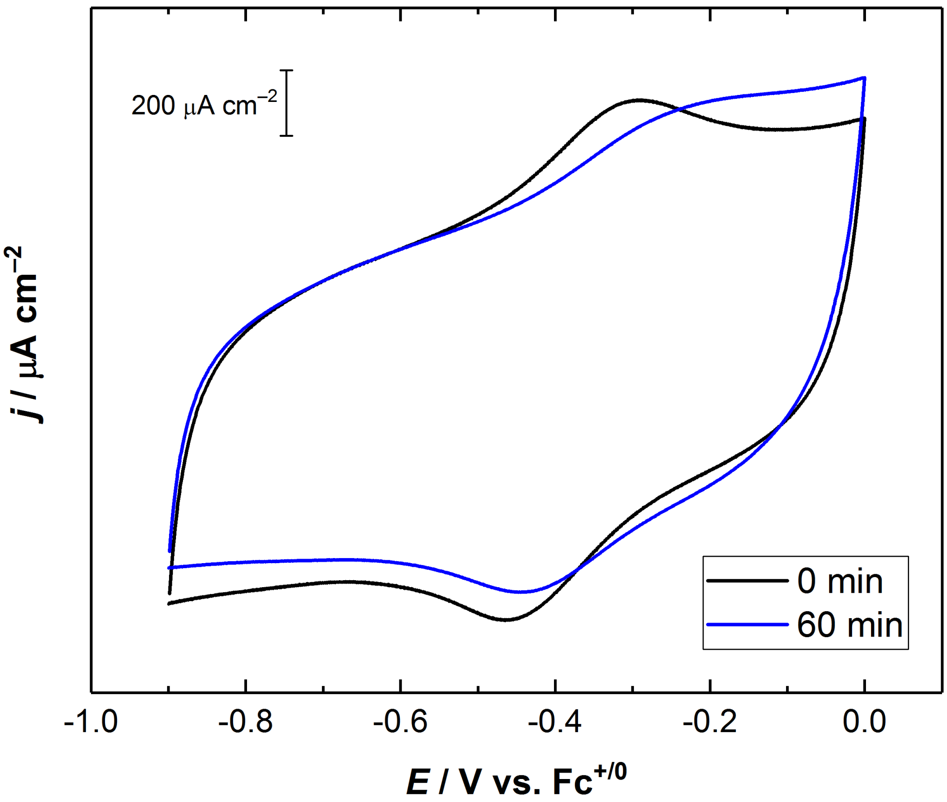

Figure S4. Cyclic voltammetry data for an electrode functionalized with $\mathbf{L^{Pyr}Ce}$ before and after soaking in electrolyte solution (0.1 M [^{n}Bu$_4$N][PF$_6$] in CH$_3$CN) for 60 minutes. Initial coverage: 7±1 nanomol/cm^{-2}. Coverage after 60 min soaking: 3±1 nanomol/cm^{-2}.

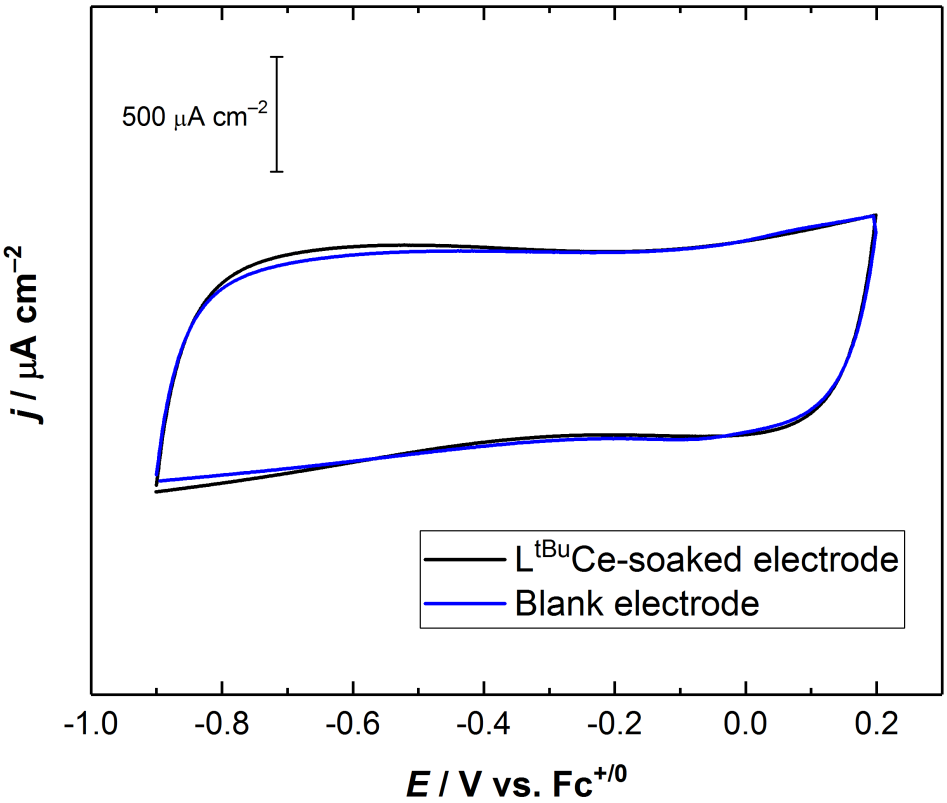

Figure S5. Cyclic voltammetry data (CH_3CN, 0.1 M [$^nBu_4N$][PF_6]) for a blank Ketjen black/HOPG electrode (blue) and for an electrode soaked in a 0.5 mM solution of **$L^{tBu}Ce$** in CH_2Cl_2 (black), highlighting the absence of any redox event in the potential window of interest in the absence of pyrene substituents on the multidentate ligand scaffold.

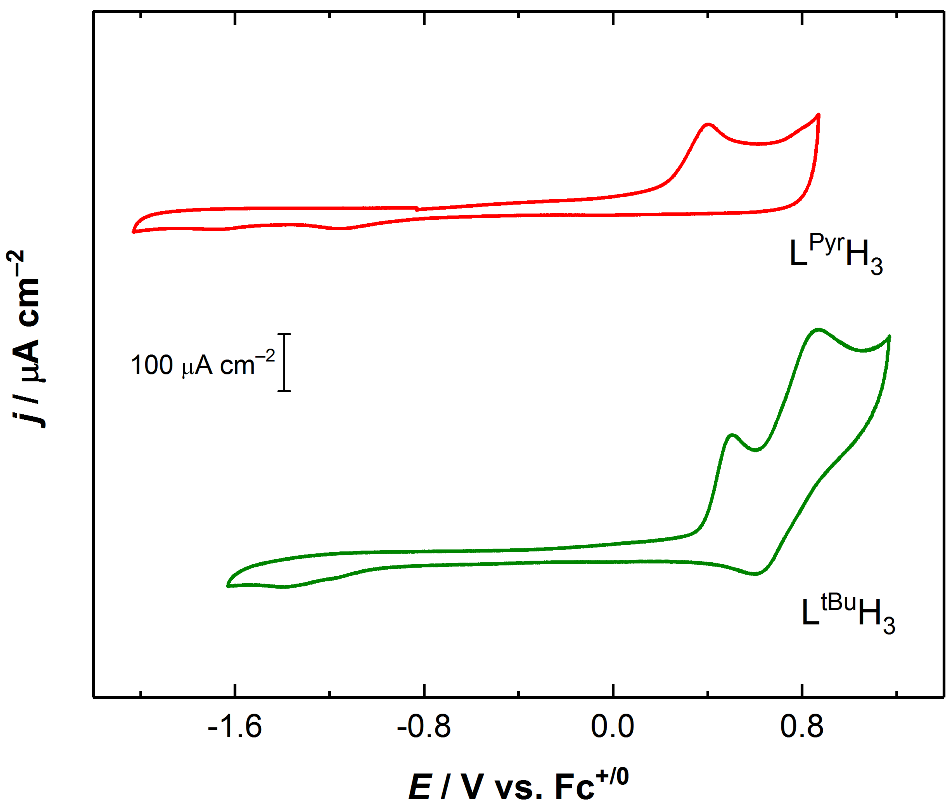

Figure S6. Cyclic voltammetry data (CH_3CN, 0.1 M [$^nBu_4N$][PF_6], 100 mV/s) for , **$L^{tBu}H_3$** (lower, green), and **$L^{Pyr}H_3$** (upper, red).

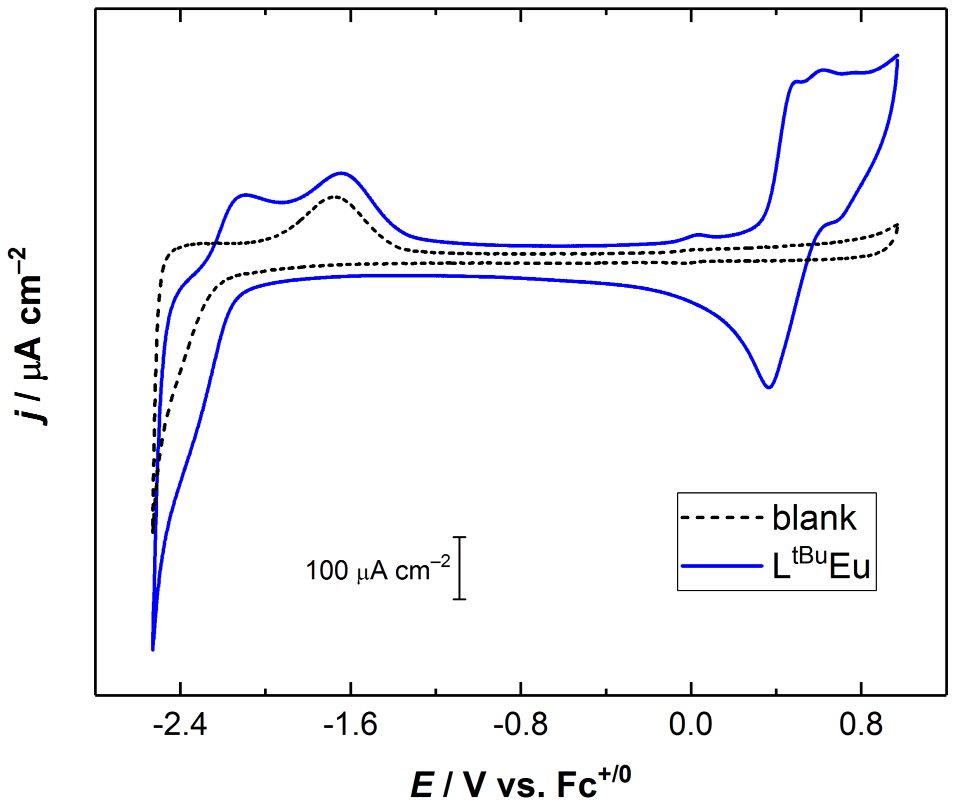

Figure S7. Cyclic voltammetry data for **L^{tBu}Eu** (blue) and blank HOPG electrode (black, dashed) in CH_3CN, 0.1 M [$^nBu_4N$][PF_6], 100 mV/s.

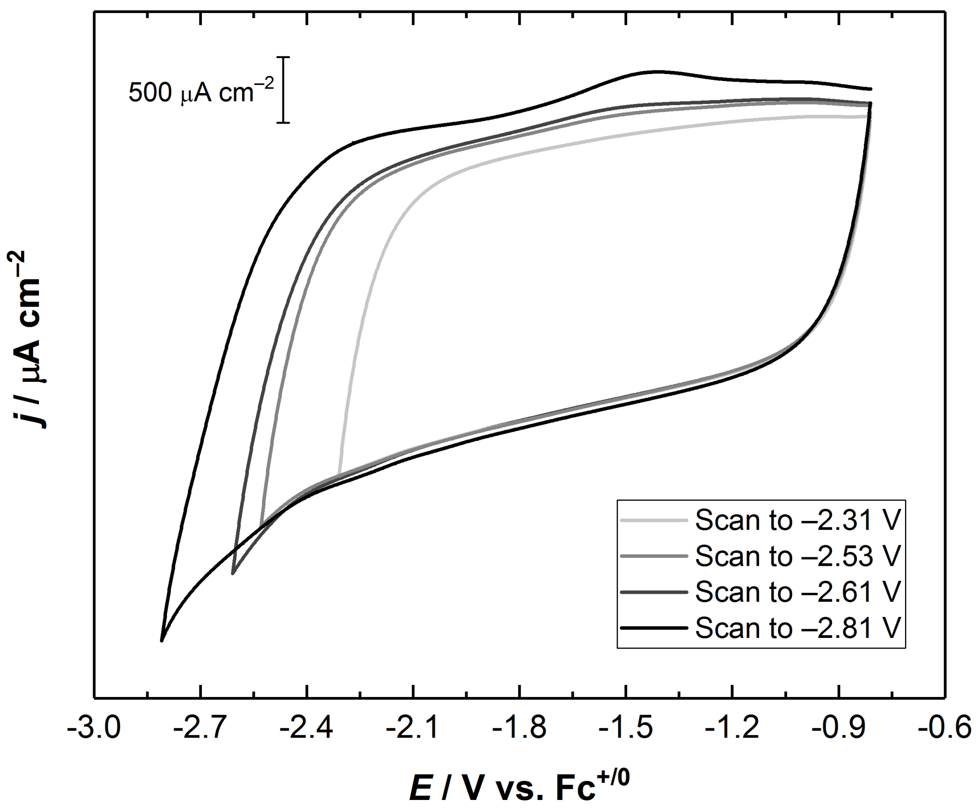

Figure S8. Cyclic voltammetry data for unfunctionalized Ketjen black electrode at increasingly negative potentials (CH_3CN, 0.1 M [$^nBu_4N$][PF_6], 100 mV/s).

X-ray Photoelectron Spectroscopy

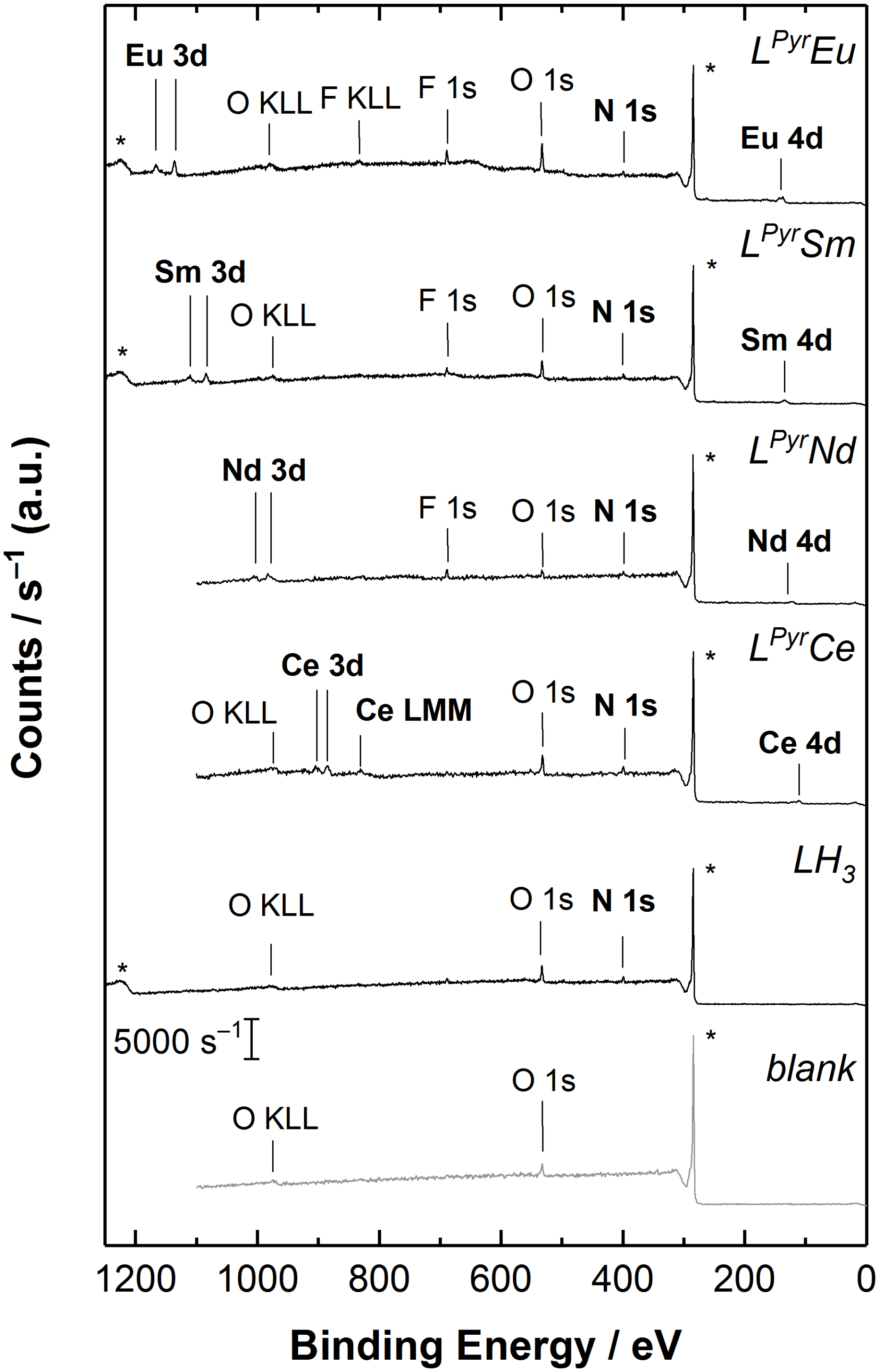

Figure S9. Survey X-ray photoelectron spectra for a blank electrode and electrodes functionalized with $\mathbf{L^{Pyr}H_3}$ and $\mathbf{L^{Pyr}M}$ complexes. Signals corresponding to the surface bound complexes are highlighted in bold. Signals corresponding to carbon (C 1s and C KLL) marked with (*).

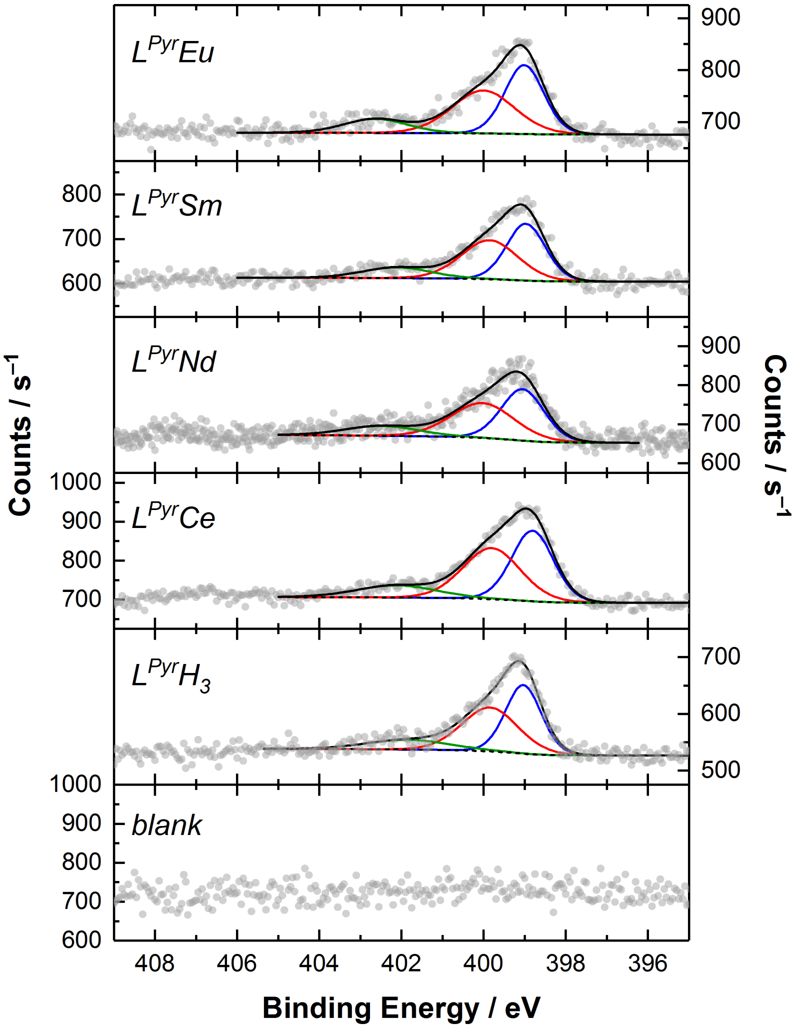

Figure S10. X-ray photoelectron spectra in the N 1s region for electrodes functionalized with $\mathbf{L^{Pyr}H_3}$ and $\mathbf{L^{Pyr}M}$ complexes. Legend: gray dots: data; dashed black lines: fitting background; blue, red and green lines: fitting curves for three distinct nitrogen environments (constrained to 3:3:1 area ratio); continuous black line: overall fit.

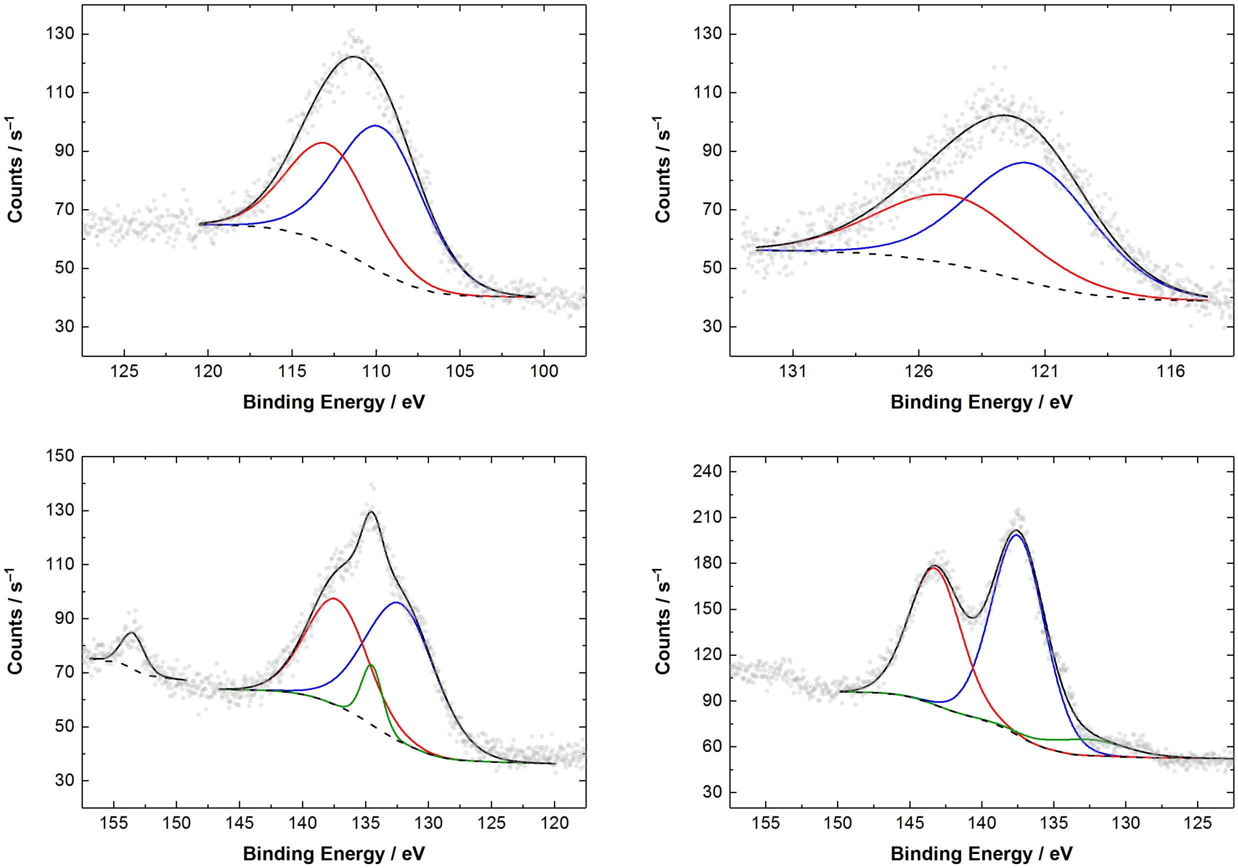

Figure S11. X-ray photoelectron spectra in the respective M 4d regions for **L^{Pyr}M** complexes. Legend: gray dots: data; dashed black lines: fitting background; blue lines: M 4d$_{5/2}$ peak fit; red lines: M 4d$_{3/2}$ peak fit (constrained to 2/3 area with respect to M 4d$_{5/2}$); green lines: shake-up and shake-down peaks fit; continuous black line: overall fit.

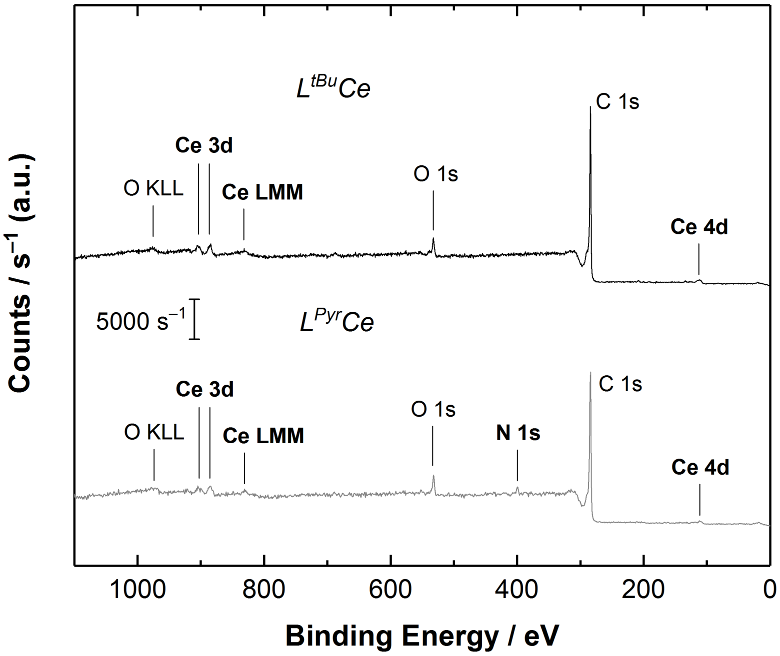

Figure S12. Survey X-ray photoelectron spectra for electrodes soaked with $\mathbf{L^{Pyr}Ce}$ (lower) and $\mathbf{L^{tBu}Ce}$ (top). Signals corresponding to the surface bound complexes are highlighted in bold. Note the lack of a signal in the N 1s region for the electrode functionalized with $\mathbf{L^{tBu}Ce}$.

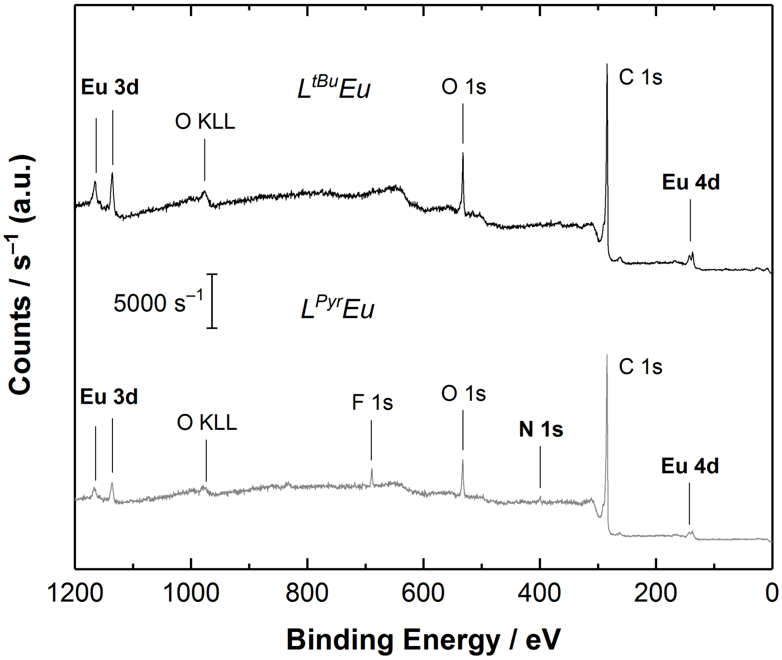

Figure S13. Survey X-ray photoelectron spectra for electrodes soaked with $\mathbf{L^{Pyr}Eu}$ (lower) and $\mathbf{L^{tBu}Eu}$ (top). Signals corresponding to the surface bound complexes are highlighted in bold. Note the lack of distinct signals in the N 1s region for the electrode functionalized with $\mathbf{L^{tBu}Eu}$.

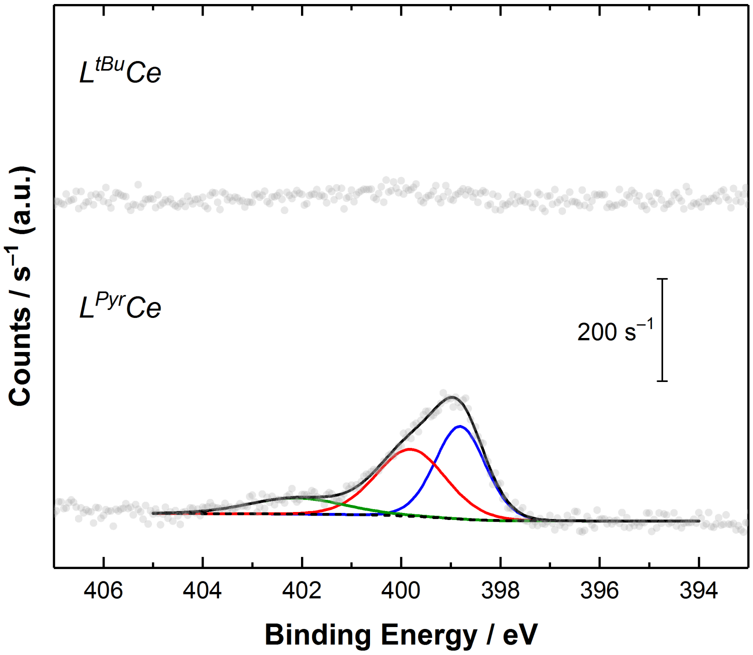

Figure S14. X-ray photoelectron spectra in the N 1s region for electrodes soaked in solutions containing **L^{Pyr}Ce** (lower) or **L^{tBu}Ce** (top). Legend: gray dots: data; dashed black lines: fitting background; blue, red and green lines: fitting curves for three distinct nitrogen environments (constrained to 3:3:1 area ratio); continuous black line: overall fit.

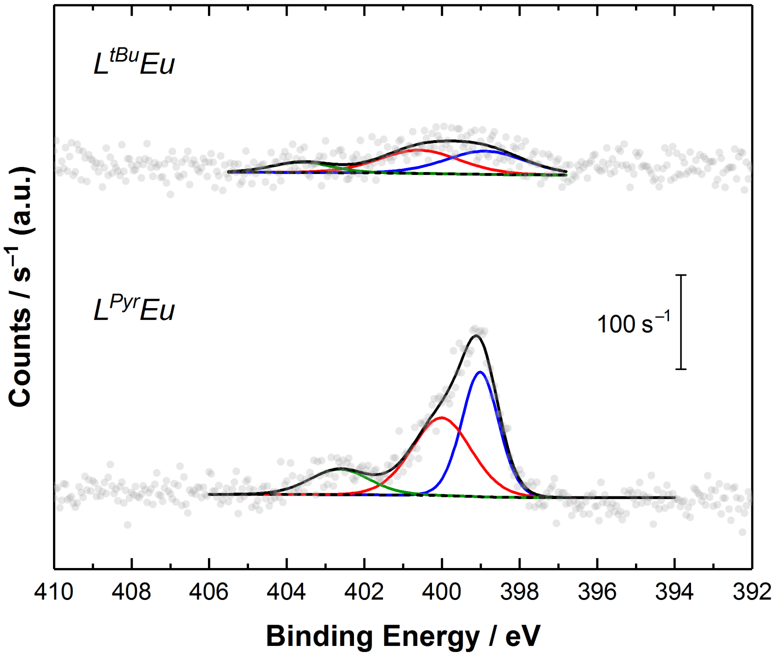

Figure S15. X-ray photoelectron spectra in the N 1s region for electrodes soaked in solutions containing **L^{Pyr}Eu** (lower) or **L^{tBu}Eu** (top). Legend: gray dots: data; dashed black lines: fitting background; blue, red and green lines: fitting curves for three distinct nitrogen environments (constrained to 3:3:1 area ratio); continuous black line: overall fit.

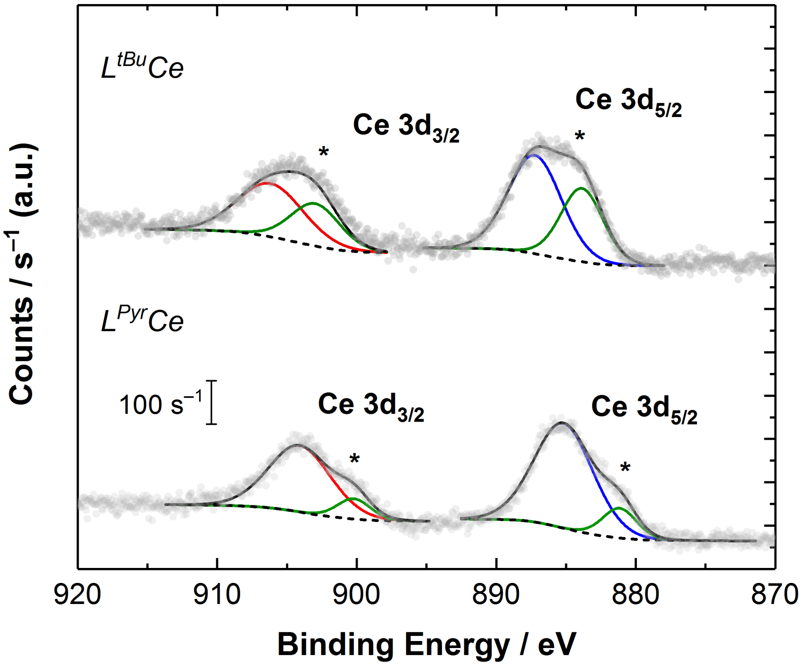

Figure S16. X-ray photoelectron spectra in the Ce 3d region for electrodes soaked in solutions of $\mathbf{L^{Pyr}Ce}$ (lower) or $\mathbf{L^{tBu}Ce}$ (top). Legend: gray dots: data; dashed black lines: fitting background; blue lines: Ce 3d$_{5/2}$ peak fit; red lines: Ce 3d$_{3/2}$ peak fit (constrained to 2/3 area with respect to Ce 3d$_{5/2}$); green lines: shake-up and shake-down peaks fit (marked with [*]); continuous black line: overall fit.

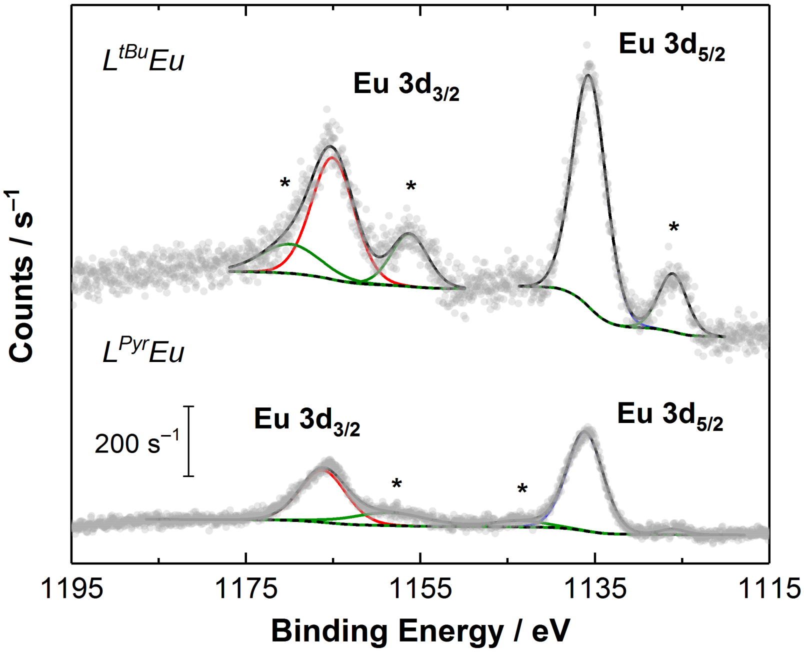

Figure S17. X-ray photoelectron spectra in the Eu 3d region for electrodes soaked in solutions of $\mathbf{L^{Pyr}Eu}$ (lower) or $\mathbf{L^{tBu}Eu}$ (top). Legend: gray dots: data; dashed black lines: fitting background; blue lines: Ce 3d$_{5/2}$ peak fit; red lines: Ce 3d$_{3/2}$ peak fit (constrained to 2/3 area with respect to Ce 3d$_{5/2}$); green lines: shake-up and shake-down peaks fit (marked with [*]); continuous black line: overall fit.

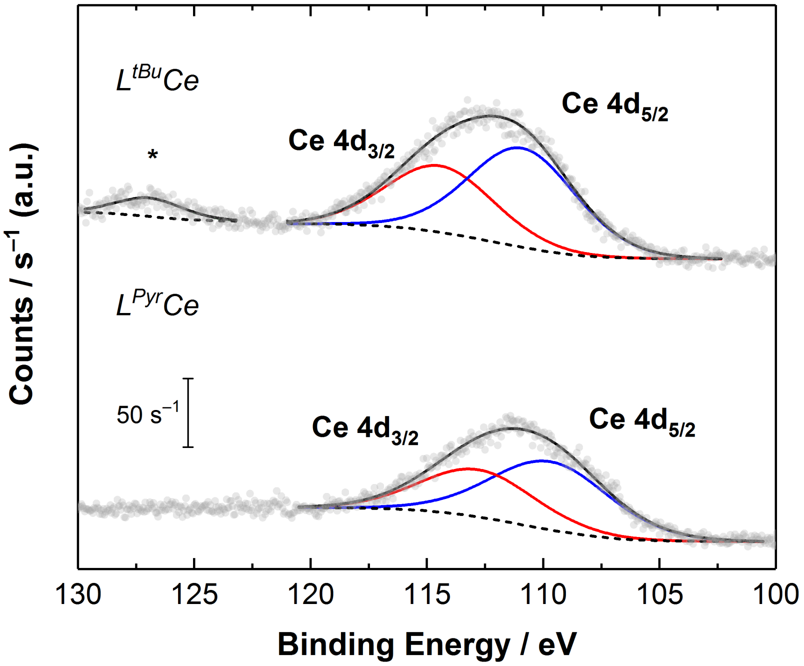

Figure S18. X-ray photoelectron spectra in the Ce 4d region for electrodes soaked in solutions of **$L^{Pyr}Ce$** (lower) or **$L^{tBu}Ce$** (top). Legend: gray dots: data; dashed black lines: fitting background; blue lines: Ce 3d$_{5/2}$ peak fit; red lines: Ce 4d$_{3/2}$ peak fit (constrained to 2/3 area with respect to Ce 4d$_{5/2}$); green lines: shake-up and shake-down peaks fit (marked with [*]); continuous black line: overall fit.

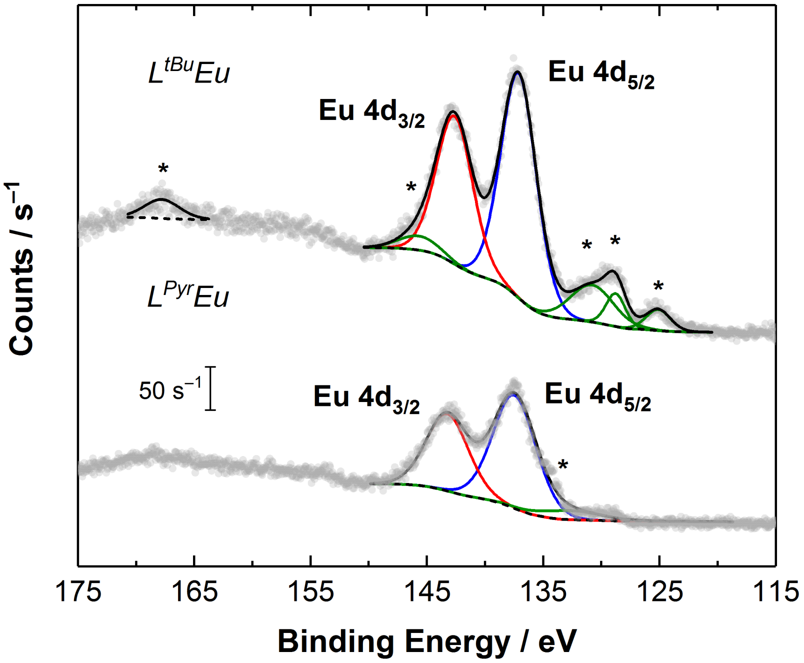

Figure S19. X-ray photoelectron spectra in the Eu 4d region for electrodes soaked in solutions of **$L^{Pyr}Eu$** (lower) or **$L^{tBu}Eu$** (top). Legend: gray dots: data; dashed black lines: fitting background; blue lines: Ce 3d$_{5/2}$ peak fit; red lines: Eu 4d$_{3/2}$ peak fit (constrained to 2/3 area with respect to Eu 4d$_{5/2}$); green lines: shake-up and shake-down peaks fit (marked with [*]); continuous black line: overall fit.

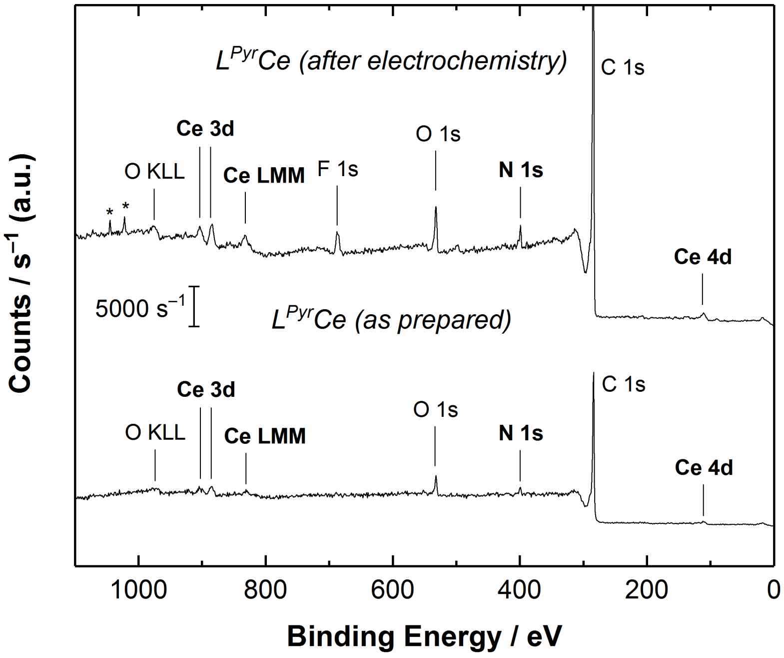

Figure S20. Survey X-ray photoelectron spectra for electrodes functionalized with **L^{Pyr}Ce** before (lower) and after (top) being utilized for electrochemistry experiments. Signals corresponding to the surface bound complexes are highlighted in bold. Signals marked with (*) correspond to Zn 2s and 2p signals due to zinc oxide being present in the sample holder.

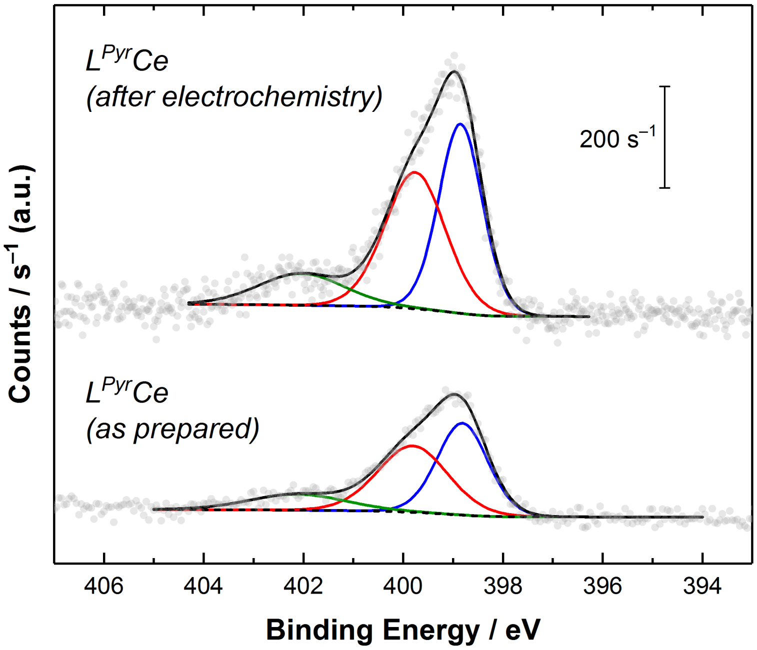

Figure S21. X-ray photoelectron spectra in the N 1s region for electrodes functionalized with **L^{Pyr}Ce** before (lower) and after (top) being utilized for electrochemistry experiments. Legend: gray dots: data; dashed black lines: fitting background; blue, red and green lines: fitting curves for three distinct nitrogen environments (constrained to 3:3:1 area ratio); continuous black line: overall fit.

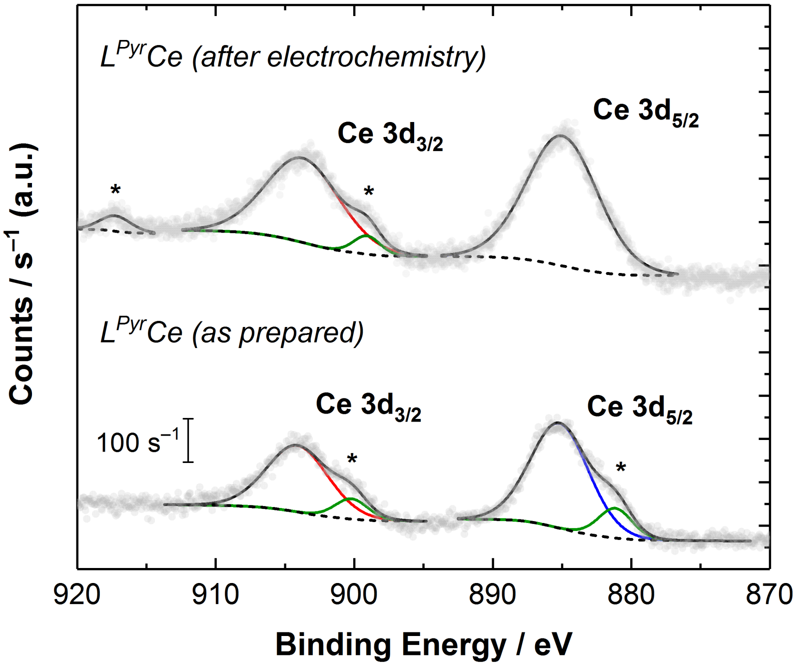

Figure S22. X-ray photoelectron spectra in the Ce 3d region for electrodes functionalized with **L^{Pyr}Ce** before (lower) and after (top) being utilized for electrochemistry experiments. Legend: gray dots: data; dashed black lines: fitting background; blue lines: Ce 3d$_{5/2}$ peak fit; red lines: Ce 3d$_{3/2}$ peak fit (constrained to 2/3 area with respect to Ce 3d$_{5/2}$); green lines: shake-up and shake-down peaks fit (marked with [*]); continuous black line: overall fit. Note: modeling of a shake-down peak for the Ce 3d$_{5/2}$ peak after electrochemistry did not result in an improved fitting, and it was therefore excluded.

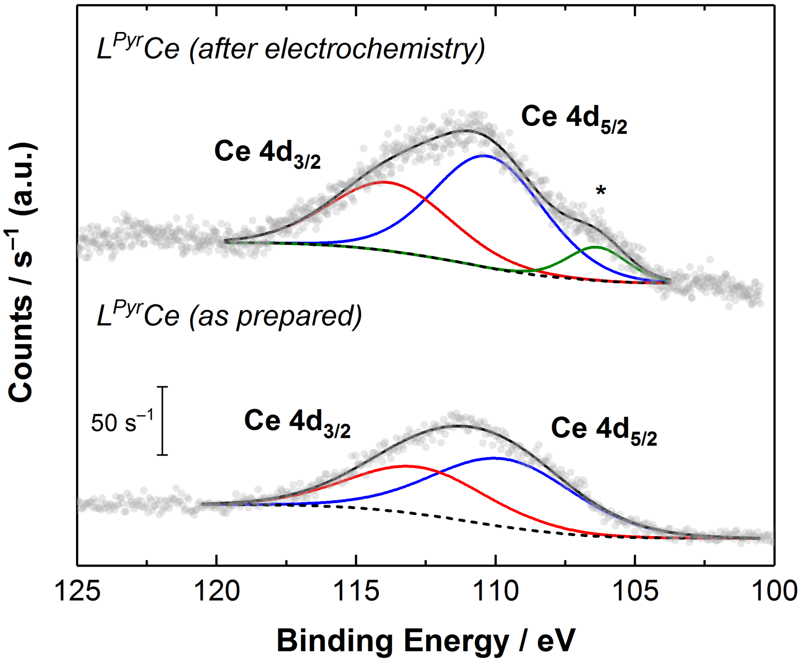

Figure S23. X-ray photoelectron spectra in the Ce 4d region for electrodes functionalized with **L^{Pyr}Ce** before (lower) and after (top) being utilized for electrochemistry experiments. Legend: gray dots: data; dashed black lines: fitting background; blue lines: Ce 3d$_{5/2}$ peak fit;

red lines: Ce $3d_{3/2}$ peak fit (constrained to 2/3 area with respect to Ce $3d_{5/2}$); green lines: shake-up and shake-down peaks fit (marked with [*]); continuous black line: overall fit.

Table S1. Comparison of binding energies (eV) for selected photoelectron peaks for electrodes functionalized with $\mathbf{L^{Pyr}Ce}$ as prepared and following electrochemical cycling. Area ratios for Ce 3d and 4d features correspond to constraints in fitting protocol

	N 1s (eV) (3:3:1 area ratio)	M $3d_{5/2,\ 3/2}$ (eV) (3:2 area ratio)	M $4d_{5/2,\ 3/2}$ (eV) (3:2 area ratio)	M 3d splitting (eV)	M 4d splitting (eV)	M/N_{axial} ratio[a]
$\mathbf{L^{Pyr}Ce}$	398.8	885.2	109.7	19.0	3.1	1.0
As prepared	399.8	904.2	112.8			
	402.1					
$\mathbf{L^{Pyr}Ce}$	398.8	885.0	110.2	18.7	3.6	0.9
After CV	399.8	903.7	113.8			
studies	402.0					

[a] Ratio of metal to unique axial N atom in $\mathbf{L^{Pyr}H_3}$ scaffold based upon integration of respective XPS signals (Ce $3d_{5/2}$ and highest binding energy N 1s signals) normalized using relative sensitivity factors (predicted ratio: 1.0).

Table S2. Comparison of binding energies (eV) for selected photoelectron peaks for electrodes functionalized with $\mathbf{L^{Pyr}M}$ and $\mathbf{L^{tBu}M}$ (M = Ce, Eu). Area ratios for M 3d and 4d correspond to constraints in fitting protocol

	N 1s (eV) (3:3:1 area ratio)	M $3d_{5/2,\ 3/2}$ (eV) (3:2 area ratio)	M $4d_{5/2,\ 3/2}$ (eV) (3:2 area ratio)	M 3d splitting (eV)	M 4d splitting (eV)	M/N_{axial} ratio[a]
$\mathbf{L^{Pyr}Ce}$	398.8	885.2	109.7	19.0	3.1	1.0
	399.8	904.2	112.8			
	402.1					
$\mathbf{L^{tBu}Ce}$	-	887.2	110.9	19.0	3.5	-
		906.2	114.4			
$\mathbf{L^{Pyr}Eu}$	399.0	1,136.1	137.5	30.0	5.8	1.2
	400.0	1,166.2	143.2			
	402.6					
$\mathbf{L^{tBu}Eu}$	398.9	1135.6	137.1	29.4	5.5	>10
	400.6	1165.0	142.6			
	403.6					

[a] Ratio of metal to unique axial N atom in $\mathbf{L^{Pyr}H_3}$ scaffold based upon integration of respective XPS signals (M $3d_{5/2}$ and highest binding energy N 1s signals) normalized using relative sensitivity factors (predicted ratio: 1.0)

NMR Spectra

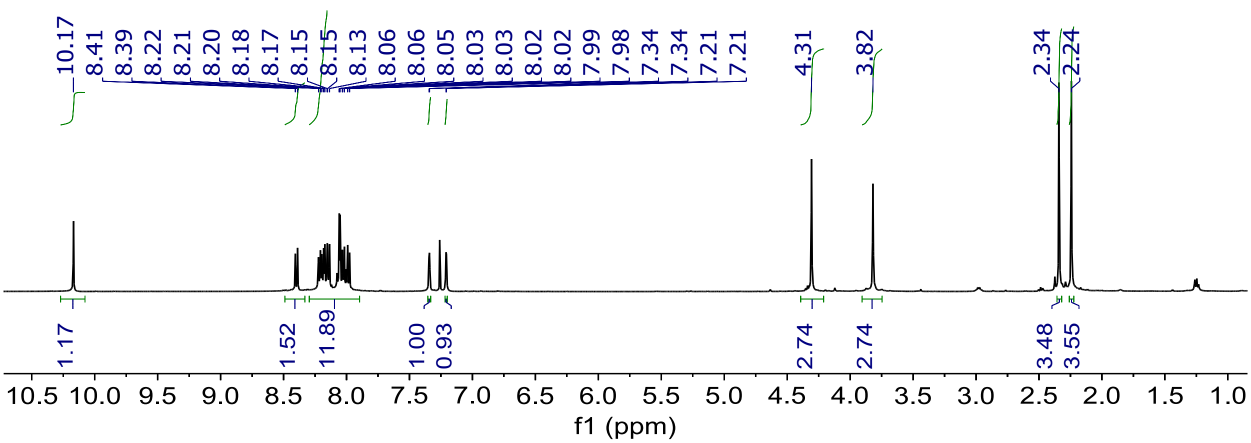

Figure S24. ^{1}H NMR spectrum (500 MHz, $CDCl_3$) of **2**.

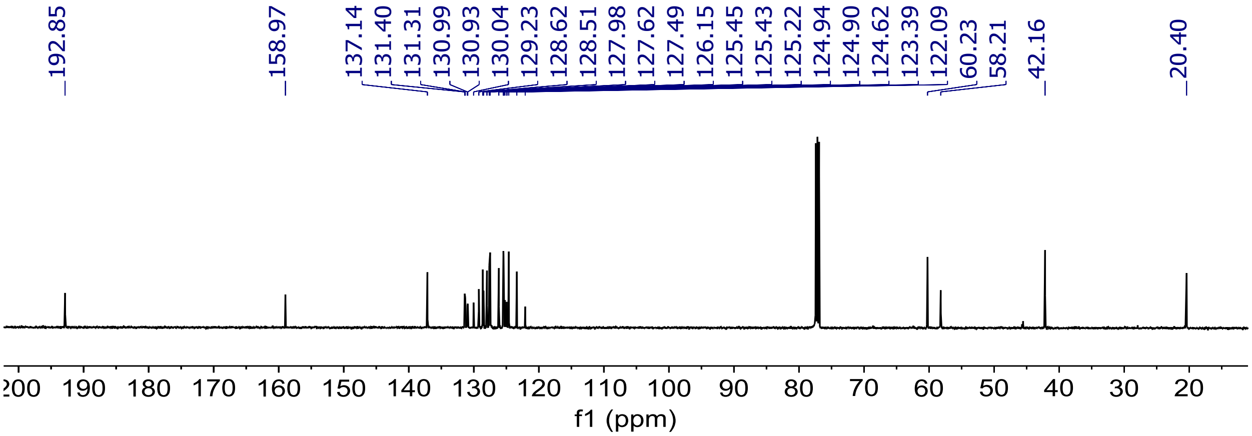

Figure S25. ^{13}C NMR spectrum (126 MHz, $CDCl_3$) of **2**.

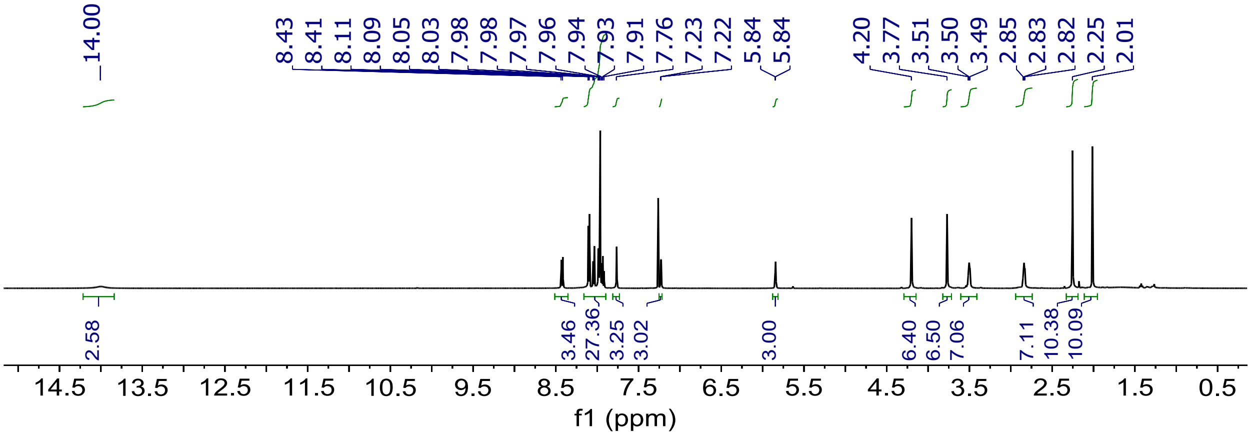

Figure S26. ^{1}H NMR spectrum (500 MHz, $CDCl_3$) of $\mathbf{L^{Pyr}H_3}$.

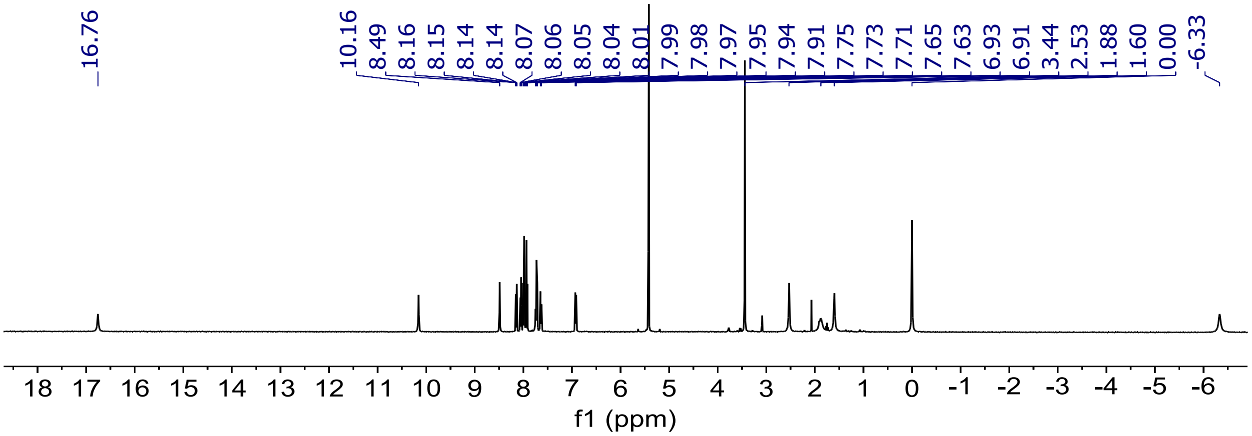

Figure S27. ^{1}H NMR spectrum (400 MHz, CD_2Cl_2) of **L^{Pyr}Ce**.

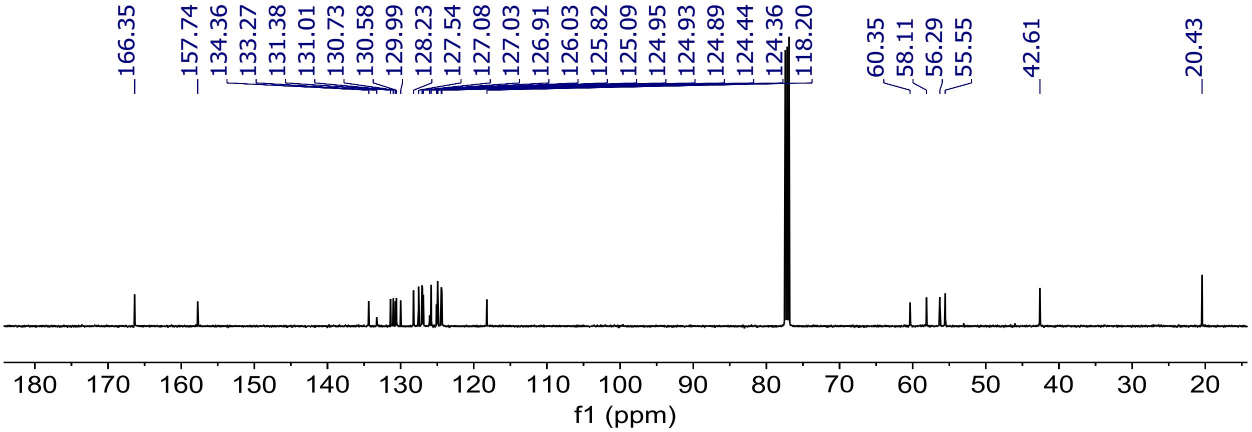

Figure S28. ^{13}C NMR spectrum (126 MHz, $CDCl_3$) of **L^{Pyr}Ce**.

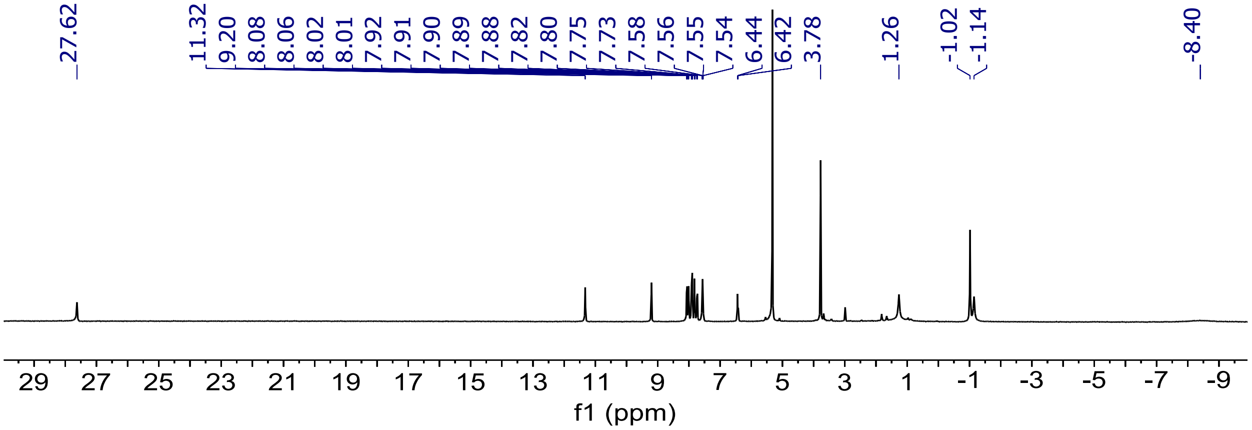

Figure S29. ^{1}H NMR spectrum (400 MHz, CD_2Cl_2) of **L^{Pyr}Nd**.

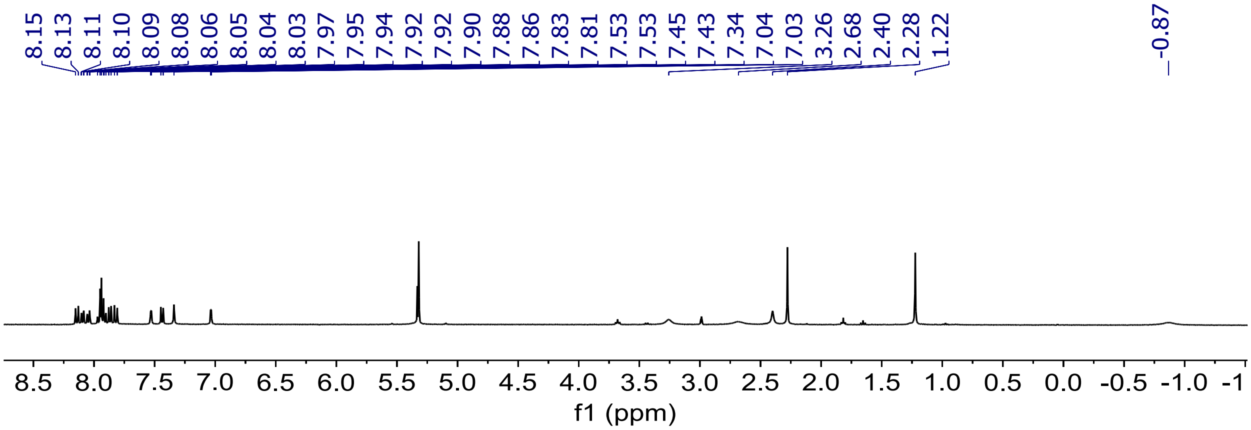

Figure S30. ^{1}H NMR spectrum (400 MHz, CD_2Cl_2) of **L^{Pyr}Sm**.

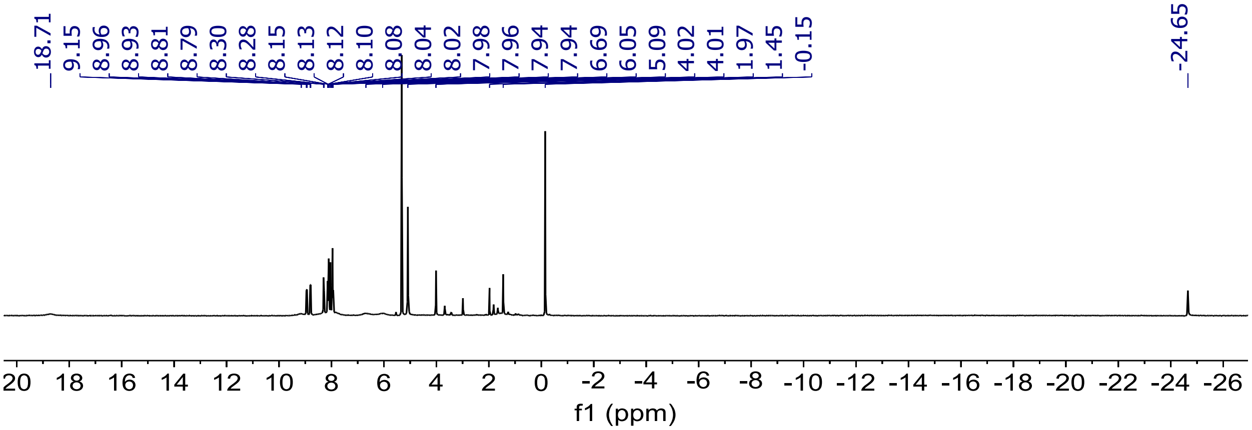

Figure S31. ^{1}H NMR spectrum (400 MHz, CD_2Cl_2) of **L^{Pyr}Eu**.

Crystallographic Information

Refinement Details

Crystals of **L^{tBu}Eu** were mounted on a nylon loop using Paratone oil under a nitrogen stream. Low temperature (200 K) X-ray data were obtained with a Bruker MicroStar microfocus rotating anode generator running at 60mA and 45kV (Cu K_α = 1.54178 Å; APEX II detector positioned at 50.0 mm and equipped with Helios multilayer mirror optics). All diffractometer manipulations, including data collection, integration and scaling were carried out using the Bruker APEXII software.[9] Absorption corrections were applied using SADABS.[10] The space groups was determined on the basis of systematic absences and intensity statistics and the structure was solved by direct methods using XS[11] (incorporated into SHELXTL) and refined by full-matrix least squares on F^2. All non-hydrogen atoms were refined using anisotropic displacement parameters. Hydrogen atoms were placed in idealized positions and refined using a riding model. The structure was refined to convergence using the Olex software package equipped with XL.[11-12]

Table S3. Crystal and refinement data

	$L^{tBu}Eu$
CCDC #	1549492
empirical formula	$C_{34}H_{50}Eu_{0.67}N_{2.67}O_2$
formula wt	629.40
T (K)	200
a, Å	16.2194(7)
b, Å	16.2194(7)
c, Å	26.9621(15)
α, deg	90
β, deg	90
γ, deg	120
V, Å^3	6142.6(6)
Z	6
cryst syst	hexagonal
space group	$P6_3/m$
ρ_{calcd}, g/cm^3	1.021
2θ range, deg	6.292 to 140.148
μ, mm^{-1}	7.569
abs corr	Multi-scan
GOOF[c]	1.156
R1,[a] wR2[b] (I > 2σ(I))	0.0450, 0.0941

[a] $R1 = \Sigma||F_o|-|F_c|| / \Sigma|F_o|$ [b] $wR2 = [\Sigma [w(F_o^2-F_c^2)^2] / \Sigma [w(F_o^2)^2]]^{1/2}$ [c] $GOOF = S = [\Sigma [w(F_o^2-F_c^2)^2] / (n-p)]^{1/2}$

Special Refinement Details for $\mathbf{L^{tBu}Eu}$.

The obtained structure for $\mathbf{L^{tBu}Eu}$ contained several disordered portions. The *tert*-butyl substituent in the position *para* to the phenoxide motif was disordered over two positions (72:28 occupancy ratio). The anisotropic parameters for the carbon atoms in the *tert*-butyl group with lower occupancy (C14A, C15A, C16A, C17A) were constrained using the EADP command using the corresponding carbon atoms in the *tert*-butyl group with higher occupancy (C1, C15, C16, C17) as template. The structure also contained large solvent-accessible voids with substantial electron density that could not be satisfactorily refined as individual solvent molecules due in part to the high symmetry of the crystal space group ($P6_3/m$). Therefore, the solvent masking tool contained in Olex^2 was used to account for this disorder.[12] Since the spectroscopic characterization of the obtained material was observed to match the literature, it was concluded that utilization of the solvent masking tool would not be disruptive to interpretation of the structural information obtained from refinement.

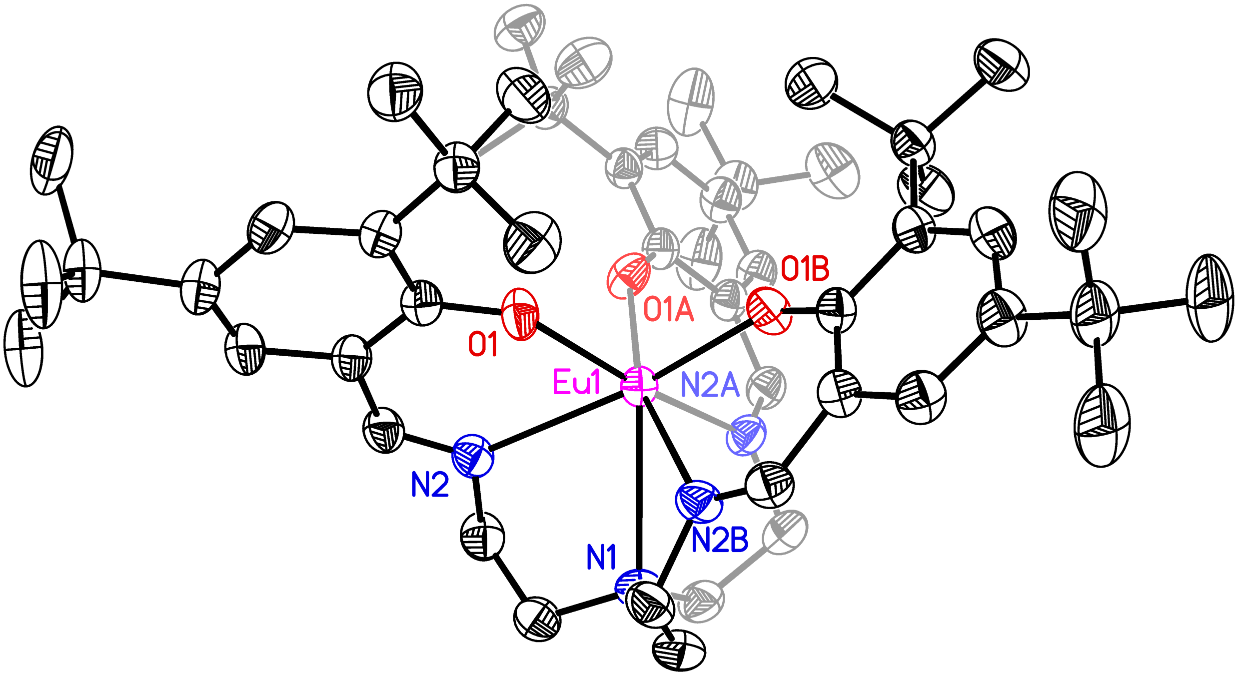

Figure S232. Full solid-state structure of $\mathbf{L^{tBu}Eu}$, side view Major orientation of disordered *para*-^{t}Bu substituents shown. Hydrogen atoms omitted for clarity. Displacement ellipsoids shown at the 50% probability level.

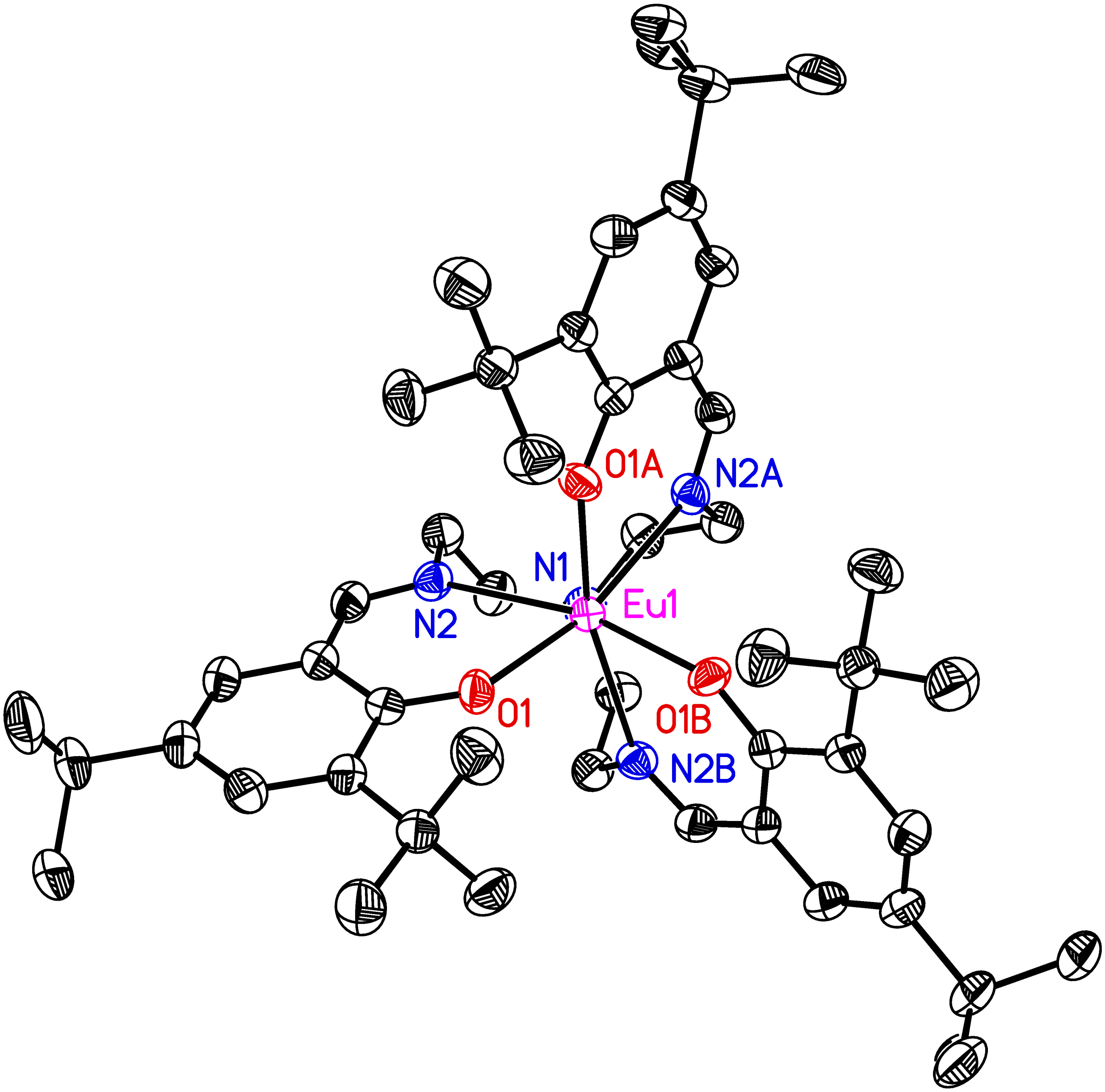

Figure S33. Full solid-state structure of **L^{tBu}Eu**, top-down view Major orientation of disordered *para*-^{t}Bu substituents shown. Hydrogen atoms omitted for clarity. Displacement ellipsoids shown at the 50% probability level.

References

(1) Chirakul, P.; Hampton, P. D.; Bencze, Z. *J. Org. Chem.* **2000**, *65*, 8297-8300.
(2) Chen, H.; Yang, H.; Xu, W. C.; Tan, Y. B. *Rsc Adv.* **2013**, *3*, 13311-13317.
(3) Bradley, D. C.; Ghotra, J. S.; Hart, F. A. *J. Chem. Soc. Dalton Trans.* **1973**, 1021-1027.
(4) Fulmer, G. R.; Miller, A. J. M.; Sherden, N. H.; Gottlieb, H. E.; Nudelman, A.; Stoltz, B. M.; Bercaw, J. E.; Goldberg, K. I. *Organometallics* **2010**, *29*, 2176-2179.
(5) Agbo, P.; Heath, J. R.; Gray, H. B. *J. Phys. Chem. B* **2013**, *117*, 527-534.
(6) Blakemore, J. D.; Gupta, A.; Warren, J. J.; Brunschwig, B. S.; Gray, H. B. *J. Am. Chem. Soc.* **2013**, *135*, 18288-18291.
(7) Gupta, A.; Blakemore, J. D.; Brunschwig, B. S.; Gray, H. B. *J. Phys.: Condens. Matter* **2016**, *28*, 1-7.
(8) Briggs, D. In *Handbook of X-ray and Ultraviolet Photoelectron Spectroscopy*; Briggs, D., Ed.; Heyden: London, 1977, p 153-182.
(9) *APEX2, Version 2 User Manual, M86-E01078,*; Bruker Analytical X-ray Systems: Madison, WI, June 2006.
(10) SADABS (version 2008/1): Program for Absorption Correction for Data from Area Detector Frames
(11) Sheldrick, G. *Acta Crystallogr., Sect. C: Cryst. Struct. Commun.* **2015**, *71*, 3-8.
(12) Dolomanov, O. V.; Bourhis, L. J.; Gildea, R. J.; Howard, J. A. K.; Puschmann, H. *J. Appl. Crystallogr.* **2009**, *42*, 339-341.